N-rGO/NiCo$_2$O$_4$ nanocomposite for high performance supercapacitor applications

G. Vignesh[1], P. Devendran[1,*], N. Nallamuthu[2], S. Sudhahar[3], and M. Krishna Kumar[4,*] (ID)

[1] Energy Physics Laboratory, Department of Physics, Kalasalingam Academy of Research and Education (Deemed to be University), Krishnankoil 626 126, India

[2] Department of Physics, Dayanada Sagar Academy of Technology and Management, Bengaluru, Karnataka 560 082, India

[3] Department of Physics, Alagappa University, Karaikudi 630 003, India

[4] Department of Physics and Electronics, CHRIST (Deemed to be University), Bengaluru 560 029, India

ABSTRACT

Spinel structured transition metals oxide GO/NiCo$_2$O$_4$ nanocomposites and nitrogen doped N-rGO/NiCo$_2$O$_4$ nanocomposites were developed. Powder X-ray diffraction investigations confirmed the structure. The bonding vibrations of the produced nanocomposites were confirmed using infrared and Raman spectroscopy. EDX analysis was used to determine the composition and element weights of the nanocomposites. The electrochemical properties of the nanomaterials were measured using 1 M KOH electrolyte. At 5mVs^{-1} scan rates, cyclic voltammetry revealed a specific capacitance (C_{sp}) of 1078.2 Fg^{-1} for N-rGO/NiCo$_2$O$_4$. The bare and nanocomposites of NiCo$_2$O$_4$, GO/NiCo$_2$O$_4$, and N-rGO/NiCo$_2$O$_4$ specific capacitance, charge-discharge capability, and cyclic stability were investigated. Energy density and power density of the N-rGO/NiCo$_2$O$_4$ nanocomposite were estimated to be 20.4 Wh kg^{-1} and 1300 W kg^{-1}, respectively. N-rGO//N-rGO/NiCo$_2$O$_4$ asymmetric supercapacitor device with E$_d$ of 14.9 Wh kg^{-1} and P$_d$ of 3500 W kg^{-1} was fabricated.

1 Introduction

Carbon traces, like global warming, pose a significant challenge to the developing world. It can be replaced by either electric vehicles (EV) or by lowering carbon traces in the atmosphere. EV is the most preferred, and research into hybrid combination-based nanocomposites is critical [1]. Because of industrialization, modern lifestyle, and large amounts of carbon emission in various ways, the demand for energy storage is constantly increasing. Because electric vehicle technology has gained popularity, the sincere search for high energy density (E_d) and high power density (P_d) storage materials has become a top priority [2]. Furthermore, a single material cannot be adequate for a wide range of applications. As a result, a variety of materials will be investigated for various types of application needs. NiCo$_2$O$_4$ has

Address correspondence to E-mail: pdevavenmani@gmail.com; krishnakumarinfo@gmail.com

recently become a research hotspot as an electrode material for supercapacitors due to its multiple redox states and low barrier to protons/cations diffusion [3–5]. Ternary metal cobaltite $NiCo_2O_4$ (NCO) has a spinal $A^{2+}B_2^{3+}O_4$ structure that can be formed by replacing one cobalt atom in Co_3O_4 with nickel. The theoretical specific capacitance of this spinel structure is 2682 Fg^{-1} [6]. Redox pairs Co^{2+}/Co^{3+} and Ni^{2+}/Ni^{3+} can move during the charge-discharge process. The importance of $NiCo_2O_4$ for energy storage applications is validated by the desired oxidation states. It has higher electrochemical activity than pure Co_3O_4 and NiO, as well as higher electronic conductivity (σ) of approximately $10^{-1} \sim 10^2$ Scm^{-1} [7]. In the regular spinel structure, divalent Ni^{2+} and trivalent Co^{3+} cations occupy tetrahedral and octahedral voids, respectively. In regular spinel, NiO_4 tetrahedra are unconnected, while CoO_6 octahedra share an edge. When tetrahedra cations move to octahedra sites, the inverse spinel is formed [8]. Transition metal oxides (TMO) are gaining popularity due to their low cost and environmental friendliness [9, 10]. TMOs have low electronic conductivity, which can be improved by using different preparation methods such as chemical, solid-state, and nanoscale methods [11].

Carbon materials with higher electronic conductivity include carbon nanotubes and graphene oxide. As a result, making nanocomposites of $NiCo_2O_4$ with graphene oxides (GO) has the potential to yield higher electronic conductivity. $NiCo_2O_4$ rich redox oxidation states provide good specific capacitance capability [12]. Reduced graphene oxide (rGO) can be chemically tuned to change its physical and chemical properties [13]. By functionalization, pentavalent nitrogen can be added to rGO. Nitrogen (N) functionalization liberates an excess of its one electron, resulting in rGO as an n-type semiconductor and increased electronic conductivity [14]. N atoms can replace the hardest carbon sites, causing significant damage to the honeycomb structure [15]. More functionalization increases defect sites and conductivity. The high surface area of GO, approximately 2630 m^2g^{-1}, is advantageous for decorating TMOs for planning hybrid materials with nitrogen functionalization indicating GO reduction [16]. The difficulties associated with $NiCo_2O_4$ nanomaterials can be overcome by employing high surface area and nitrogen functionalized graphene oxide with higher conduction [17]. The combination of pseudocapacitive TMOs

and GOs electric double layer capacitance (EDLC) results in synergistic hybrid effects of its physical properties [18]. There are numerous methods for doping nitrogen through the functionalization process, including hydrazine [19, 20], hexamine [21], urea [22], uric acid [23], ammonia [20, 24]. Hydrazine and ammonia functionalized N-rGO was used in a sonochemical process to produce a $NiCo_2O_4$/N-rGO nanocomposite with a maximum specific capacitance of 618 Fg^{-1} at a current density of $4Ag^{-1}$ [20]. So far, N-doped graphene oxide (N-rGO), particularly from urea with $NiCo_2O_4$ nanocomposite, has not been studied.

The goal of this study is to functionalize graphene oxide and prepare the N-rGO/$NiCo_2O_4$ nanocomposite for supercapacitor applications. The presence of N in N-rGO/$NiCo_2O_4$ can effectively anchor metal ions to promote uniform dispersion for conduction, resulting in significantly increased ionic conductivity [3]. An electrochemical energy storage system's positive characteristics include a good specific capacitance, a wider temperature tolerance, maximum power densities, and low self-discharge (EES). $NiCo_2O_4$ has been mixed to create a nanocomposite and examined for its exceptional theoretical specific capacitance and high conduction N-rGO. The X-ray diffraction, spectroscopic, morphological, and electrochemical data of N-rGO/$NiCo_2O_4$ are discussed in this paper. Asymmetric supercapacitor device N-rGO//N-rGO/$NiCo_2O_4$ electrochemical performance is also reported.

2 Experimental

2.1 Materials

The analytical grade of reagents of graphite powder (98%), sulfuric acid (98%), hydrogen peroxide (30%), hydrochloric acid (35%), cobalt nitrate hexahydrate (98%), nickel nitrate hexahydrate (99%), sodium hydroxide (98%), urea (99.5%) and ethanol used to synthesis of N-rGO/$NiCo_2O_4$ nanocomposite. All the reagents were used as received.

2.2 GO, N-rGO, N-rGO/$NiCo_2O_4$ and N-rGO/$NiCo_2O_4$ synthesis

By using a modified version of Hummers' process, graphene oxide (GO) was produced from graphite

flakes [25]. By allowing nickel nitrate and cobalt nitrate to react in a 2:1 ratio with the addition of sodium hydroxide, $NiCo_2O_4$ nanoparticles were created. Expected intermediate of metal hydroxides is allowed to dry before being calcined at 350 °C for four hours. Phase transitions from hydroxide to nickel cobaltite are made possible by the calcination process. For $GO/NiCo_2O_4$, the same method utilized for $NiCo_2O_4$ was applied by adding sonicated GO solution along with the precursors. For the synthesis of $GO/NiCo_2O_4$, precursors of $NiCo_2O_4$ and GO were employed in a ratio of about 1:4. On the opposite side, a hydrothermal technique was used to dope nitrogen into graphene oxide for 12 h at 180 °C. N-rGO, a hydrothermal product, is used to make $N-rGO/NiCo_2O_4$ nanocomposite, by following the method same as $GO/NiCo_2O_4$ nanocomposite. Figure 1 shows a schematic depiction of the $N-rGO/NiCo_2O_4$ synthesis process. All of the nanomaterials were collected, dried, and utilized for characterization.

2.3 Methods

The powder X-ray diffraction pattern of $NiCo_2O_4$, $GO/NiCo_2O_4$, and $N-rGO/NiCo_2O_4$ nanoparticles (NPs) was examined using a Bruker D8 advance ECO equipment to determine their crystallinity. To identify the vibrational frequencies of the groups, present in the synthesized nanomaterials, infrared and Raman vibrational spectroscopy were used. It aids in drawing conclusions about the changes made to the decrease of graphene oxide and its presence in nanocomposites (NPs). SEM images of the surface morphology of the produced nanomaterials were taken in order to comprehend the exterior architecture and correlate it with the physical and chemical properties. Utilizing a ZEISS EVO 18 A type instrument, it was captured. In order to identify and map the elements present in the produced nanomaterials, energy dispersive X-ray spectroscopy (EDX) was used. The electrochemical characteristics of GO, N-rGO, $NiCo_2O_4$, $GO/NiCo_2O_4$, and $N-rGO/NiCo_2O_4$ in 1 M KOH electrolyte were examined using a CHI6008E model three electrode system.

2.4 Fabrication of electrodes and N-rGO// N-rGO/NiCo₂O₄ supercapacitors

The working electrodes of GO, N-rGO, $NiCo_2O_4$, $GO/NiCo_2O_4$, and $N-rGO/NiCo_2O_4$ were made using 1 cm^2 nickel foil as follows. Nickel foil's surface was rubbed clean and etched to prepare it for binding with the active material. In an 80:10:10 weight ratio, activated carbon, $N-rGO/NiCo_2O_4$ NPs, and Polyvinylidene fluoride (PVDF) were added. A drop of N-methyl-2-pyrrolidone (NMP) was added after it had been thoroughly blended. On the nickel foil that had been etched, a thin film of a prepared paste-type substance was applied using a straightforward casting technique. Every electrode of the produced NPs and NC was prepared in a similar manner. At 80°C, all the electrodes were dried. KOH electrolyte containing 1 M was prepared. The electrochemical

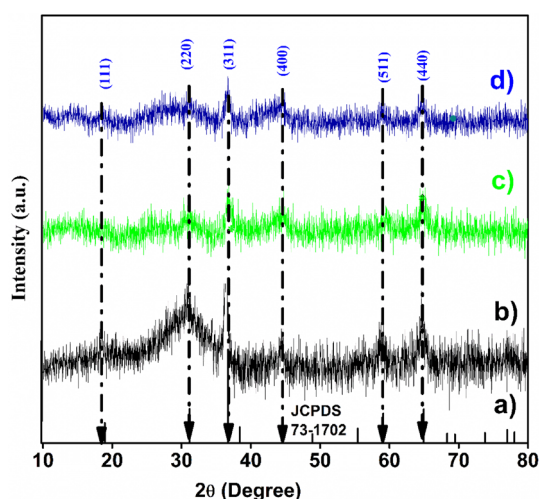**Fig. 1** Schematic diagram of $N-rGO/NiCo_2O_4$ synthesis
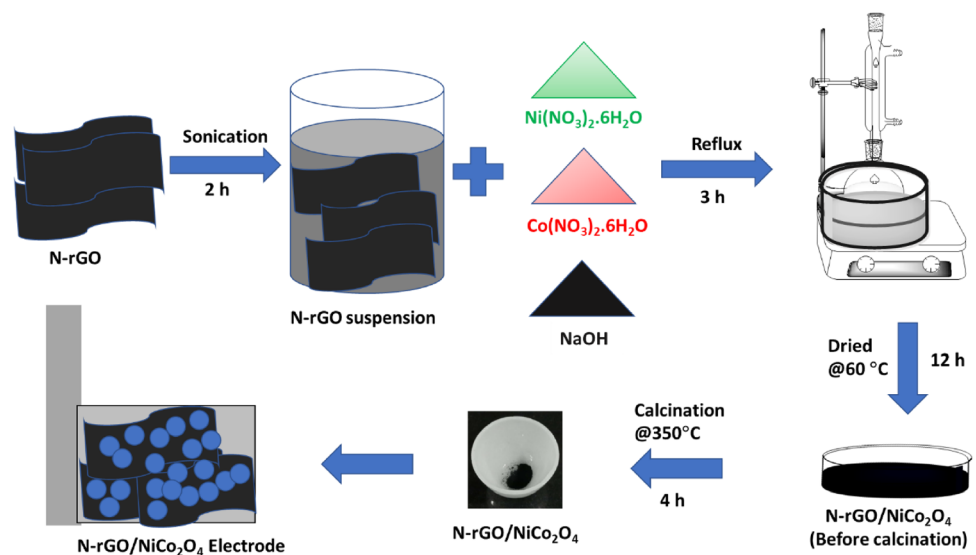
analysis of all the prepared electrodes was performed, and the findings were examined.

3 Results and discussion

3.1 X-ray diffraction of pattern

Studies on the, $NiCo_2O_4$, $GO/NiCo_2O_4$, and $N-rGO/NiCo_2O_4$ nanomaterials were done using powder X-ray diffraction. $NiCo_2O_4$ nanoparticles were proven to be in a cubic crystalline phase with Fd-3 m space group and m-3 m point group using JCPDS data # 73-1702. The crystalline phase of the synthesized nanocomposites was verified using the powder X-ray diffraction data peak angles and intensities by comparing with reference patterns [26]. The diffraction angles for the main $NiCo_2O_4$ planes (111), (220), (311), (400), (511), and (440) were correctly indexed. In comparison to pure $NiCo_2O_4$, the peaks in nanocomposites of $GO/NiCo_2O_4$ and $N-rGO/NiCo_2O_4$ are also present. This demonstrates the presence of the crystalline $NiCo_2O_4$ phase in the produced nanocomposites as shown in Fig. 2a–d. $GO/NiCo_2O_4$ and $N-rGO/NiCo_2O_4$ diffraction patterns were compared to powder X-ray patterns of GO and N-rGO from previous studies [27]. The fact that (002) and (001) planes exist proves that graphene oxides were reduced to rGO in this instance and were doped with nitrogen (N). The lack of GO, N-rGO planes in $GO/NiCo_2O_4$ and $N-rGO/NiCo_2O_4$ may be

due to a low quantity in the nanocomposite and that the nickel cobaltite plane peaks predominate. Since the formation energy of this spinel structure is lower than any other possible, the positions of the elements nickel and cobalt in the tetrahedral and octahedral forms won't be disturbed, resulting in a stable crystalline structure [28, 29]. In the use of the electrical field during electrochemical applications, it can be helpful and reversible in negative scans. Due to the synergetic interaction between layers of graphene oxide and nickel cobaltite the nanocomposite's crystallite sizes were developed. The production of the $N-rGO/NiCo_2O_4$ nanocomposite was thus confirmed by the powder X-ray diffraction analysis.

3.2 Spectral studies

FTIR and Raman spectra were acquired for the synthesized samples in this study in order to confirm the authenticity of the carbon compounds. FTIR spectra of the synthesized nanomaterials are shown in Fig. 3a–c. A prominent peak at $1394\ cm^{-1}$ and $1548\ cm^{-1}$ confirms the graphitic structure's C–N stretching and N–H vibration [30]. The aromatic carbon atoms are replaced by nitrogen atoms, which decrease to form reduced graphene oxide [31]. An indicator of the C–O–C epoxy three membered functional stretching vibration, which is present in both, is a peak at $1224\ cm^{-1}$ and $1186\ cm^{-1}$ for GO, N-rGO. The creation of replaced or defect sites is indicated by the shift in the epoxy vibration's peak position for N-rGO [32, 33]. The metal oxygen peaks, such as Ni–O and Co–O in the tetra and octahedral
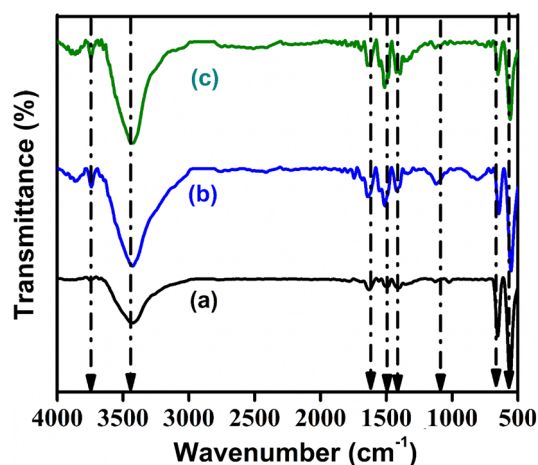

Fig. 2 Powder X-ray diffraction patterns of (a) JCPDS card no.73-1702 ($NiCo_2O_4$), (b) $NiCo_2O_4$, (c) $GO/NiCo_2O_4$, (d) $N-rGO/NiCo_2O_4$

Fig. 3 FTIR spectrum of (a) $NiCo_2O_4$ (b) $GO/NiCo_2O_4$, (c) $N-rGO/NiCo_2O_4$

voids, are represented by the peaks between 555 and 560 cm^{-1} [29]. All of the produced materials showed a broad peak at 3415–3435 cm^{-1}, indicating the presence of O–H starching vibrations. O–H groups deformation vibrations were found in the GO and N-rGO at 1410–1425 cm^{-1}, but they were not noticeable in nanocomposites. Peaks at 1699 cm^{-1} in N-rGO, 1741 cm^{-1} in N-rGO/NiCo$_2$O$_4$, 1745 cm^{-1} in GO/NiCo$_2$O$_4$, and 1745 cm^{-1} in GO/NiCo$_2$O$_4$ indicated the vibrations of the C–O–O–H group in the graphitic structure and the attachments of O–H molecules [34]. Raman spectroscopy confirms the forms of GO, N-rGO, and its nanocomposites, similar to infrared spectroscopy. The existence of GO and N-rGO in the synthesized nanocomposites has been confirmed by referencing their Raman spectra from our past investigations [27]. Because the sp^2 carbon was fractured at the graphitic structures and defect sites were generated, the intensity of the GO's D band changed. G band intensity simultaneously lowers, indicating the distortion of it [35]. For GO and N-rGO, the $I_{(D)}/I_{(G)}$ ratio assessment was determined to be 0.91 and 1.1, respectively. Additionally, the efficient doping of nitrogen into the reduced graphene oxide is shown by the shift of the G band to the lower energy. Shift also suggests that there are less 2D layers of graphene or that exfoliation occurred as a result of the nitrogen atoms being inserted into the graphitic carbon structure. Actual D and G bands for GO and N-rGO, respectively, were discovered at 1342.9 cm^{-1}, 1354.9 cm^{-1}, and 1590.3 cm^{-1}, 1584.8 cm^{-1} [27]. The Raman spectrum for the nanocomposites of GO/NiCo$_2$O$_4$ and N-rGO/NiCo$_2$O$_4$ are shown in Fig. 4a, b, and the intensities were reduced because of the lower fraction of GO and N-rGO in the metal oxide nanocomposites [36, 37]. However, it can be seen in FTIR spectra. Thus, the existence of GO, reduction of GO to N-rGO, and creation of the nanocomposites were confirmed by the infrared and Raman spectra.

3.3 Morphological studies

SEM was used to examine the surface architectural arrangement of NiCo$_2$O$_4$ nanoparticles on graphene oxide and reduced graphene oxide. The surface overview of all the prepared nanomaterials is shown in Fig. 5a–f. It shows that a small NiCo$_2$O$_4$ nanosheets-like morphology was discovered. From our earlier work, we note that the SEM images of GO and
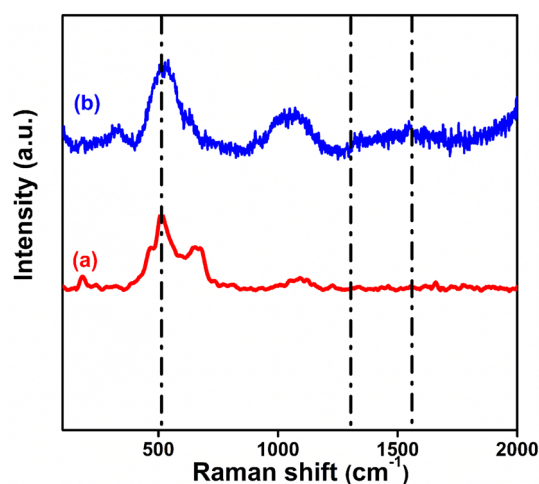
Fig. 4 Raman spectrum of (a) GO/NiCo$_2$O$_4$ (b) N-rGO/NiCo$_2$O$_4$

N-rGO show that the earlier one is slightly thicker than the later one, indicating that the nitrogen reduction process exfoliated the graphene oxide sheets [27]. The fact that the earlier one is slightly thicker than the later one demonstrates that the graphene oxide sheets were exfoliated as a result of the nitrogen reduction process. Exfoliation by deoxygenation can be accomplished concurrently with the temperature treatment used to calcine the NiCo$_2$O$_4$ and graphene oxide [38, 39]. The graphene oxide's conductivity is increased by removing oxygen from it. SEM photos show the reduced graphene oxide with nitrogen doping in a sheet-like shape. In 1 μm magnification of the specimen sample, Fig. 5e–f clearly depicts the dispersion of NiCo$_2$O$_4$ nanosheets. The NiCo$_2$O$_4$ nanosheets are dispersed across the two-dimensional N-rGO sheets as seen in its 300 nm enlarged images. The synergetic impact of NiCo$_2$O$_4$ nanosheets response to the applied electric potential will be easier at the high conduction N-rGO sheets, according to the examination of the SEM pictures of N-rGO/NiCo$_2$O$_4$ nanocomposite. All of the produced nanomaterials and nanocomposites' energy dispersive X-ray spectra are displayed in Fig. 6a–c. The nanomaterials NiCo$_2$O$_4$, GO/NiCo$_2$O$_4$, and N-rGO/NiCo$_2$O$_4$ all showed X-ray emission intensities. All of the contributing constituents in the nanomaterials received the max intensity. N-rGO's peak intensity was discovered, which proved that it had been successfully doped. The percentages of the elements present in the sample are shown in the inset figures of EDX spectra. The mapping of the area used for EDX is displayed in Fig. 7a–c in several colour
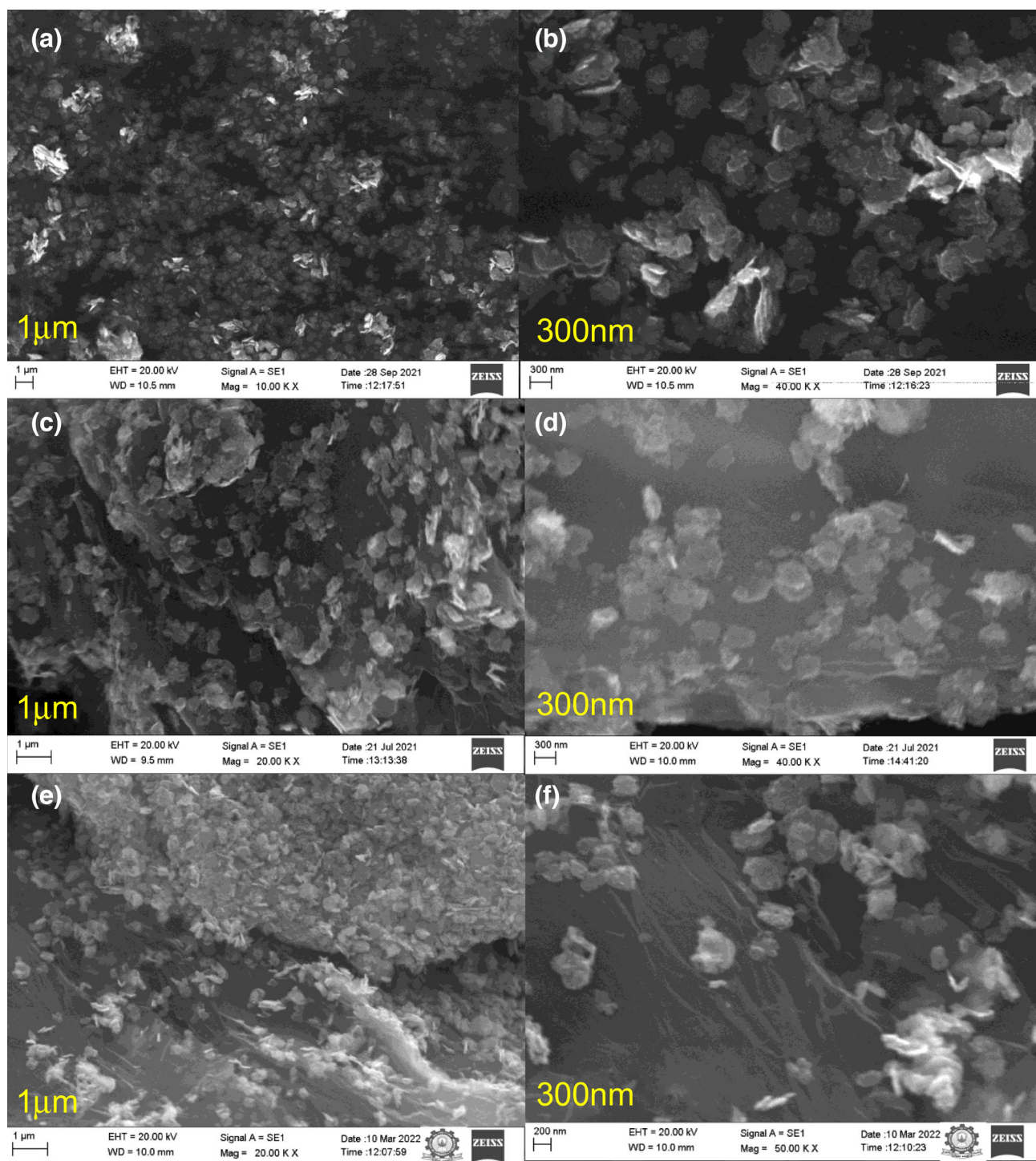
Fig. 5 SEM images of **a**, **b** $NiCo_2O_4$ at 1 μm, 300 nm, **c**, **d** $GO/NiCo_2O_4$ at 1 μm, 300 nm, **e**, **f** N-rGO/$NiCo_2O_4$ at 1 μm, 200 nm

schemes. All the components that are present in the produced nanomaterials are distributed uniformly. This suggests that nanocomposites are being formed rather than blends.

# 4 Electrochemical analyses

4.1 Cyclic voltammetry and GCD analysis

For all measurements involving electrochemical analysis, 1 M KOH electrolyte contains an Ag/AgCl
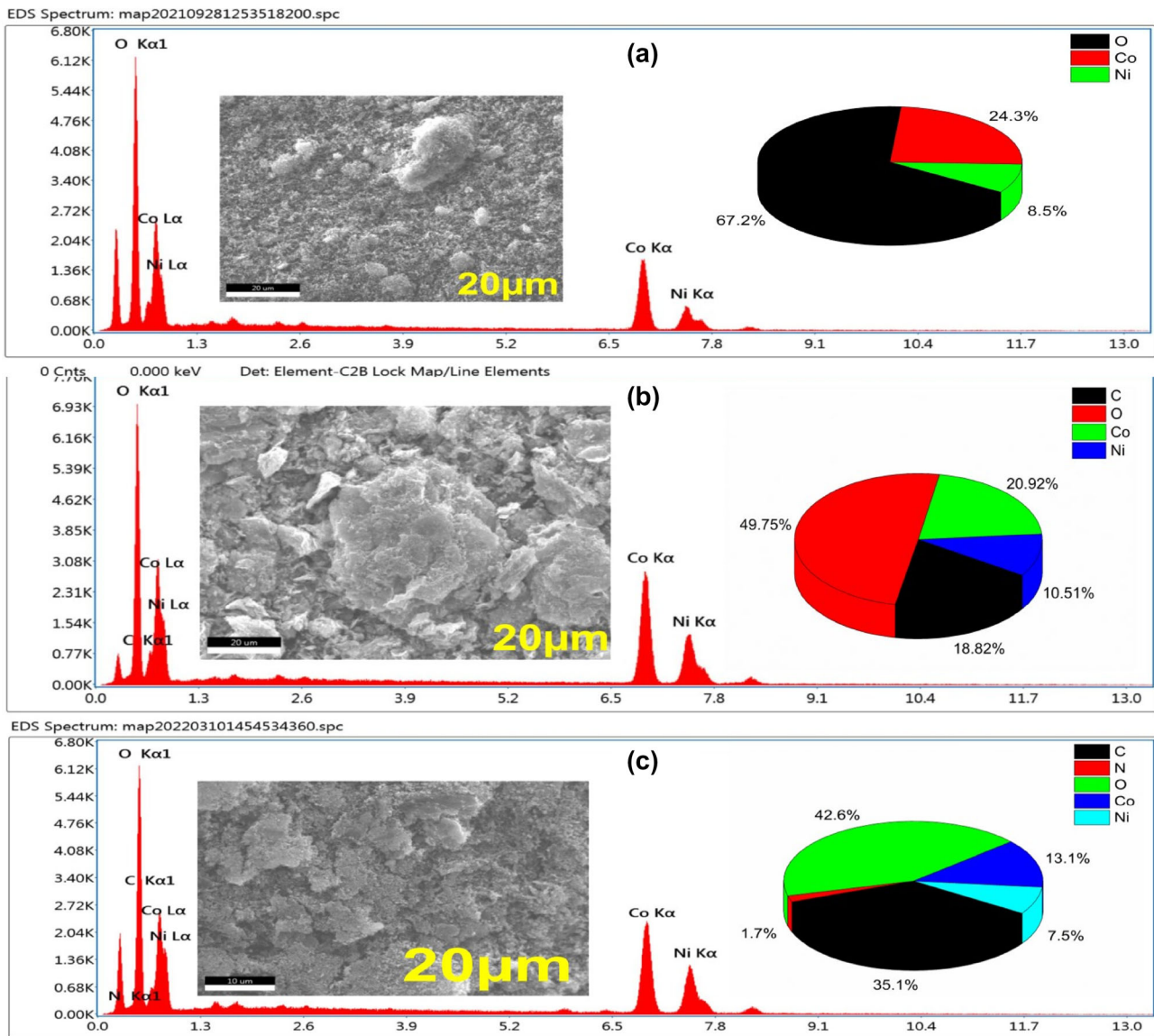
Fig. 6 EDX spectrum of **a** $NiCo_2O_4$, **b** $GO/NiCo_2O_4$, **c** N-rGO/ $NiCo_2O_4$

reference electrode. The graphene oxide electrode had an anodic potential of up to 0.9 V, while the N-rGO electrode outperformed it with a negative potential of up to 1 V and electric double layer capacitance (EDLC). The cyclic voltammetry results of spinel $NiCo_2O_4$ nanosheets and those nanocomposites are shown in Fig. 8a–d. The applied voltage scan rates ranged from $5 mVs^{-1}$ to $100 mVs^{-1}$, and the graph depicts how electrodes behave with respect to the corresponding scan rates. $NiCo_2O_4$ nanosheets exhibit pseudocapacitance, with a maximum capacitance of 227.7 Fg^{-1} at 5 mVs^{-1}, as shown in Fig. 8a. At the same scan rate, $GO/NiCo_2O_4$ nanocomposites

had 545 Fg^{-1}, while N-rGO/$NiCo_2O_4$ had 1078.2 Fg^{-1}. This demonstrates the faster faradic reaction at the interface of the solution and electrode. Due to the accessible penetration depth of the sites at the electrode, lower scan rates have higher specific capacitances and higher scan rates have lower. Because greater scan rates do not have enough time, it is because lower scan rates do [40]. The cyclic voltammetry results for $NiCo_2O_4$, $GO/NiCo_2O_4$, and N-rGO/$NiCo_2O_4$ showed oxidation and reduction redox peaks. Pseudocapacitance $NiCo_2O_4$ and EDLC graphene oxide produced hybrid capacitance effects by increasing current (I) conduction and the CV
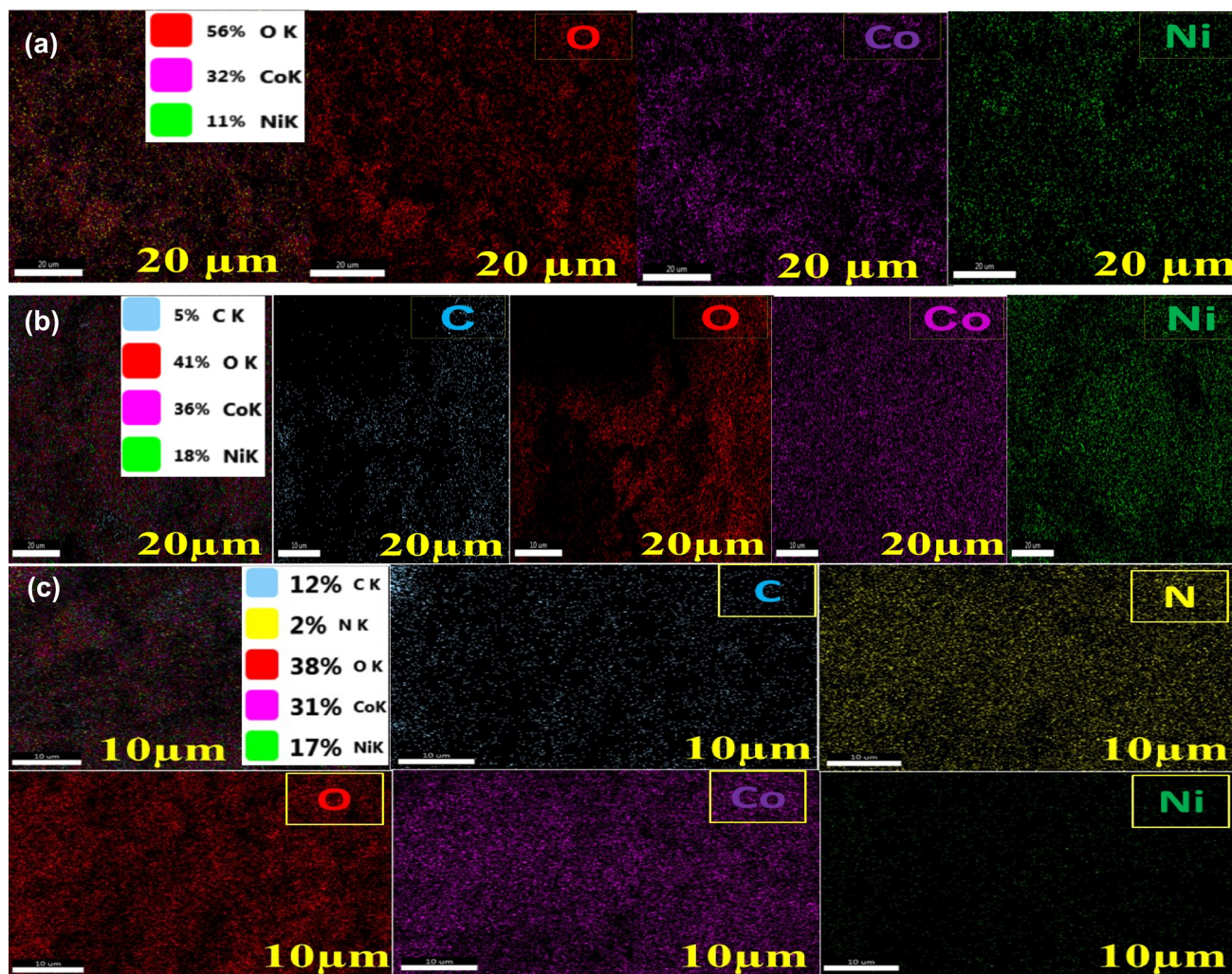
Fig. 7 Elemental mapping analysis of **a** NiCo$_2$O$_4$, **b** GO/NiCo$_2$O$_4$, **c** N-rGO/NiCo$_2$O$_4$

curve in a synergistic manner. Compared to the other electrodes, the N-rGO/NiCo$_2$O$_4$ electrode transports mass and diffusion more quickly at the solution electrode interface. N-rGO's nitrogen's free electrons make it easier for oxidation and reduction to occur more quickly at the solution-electrode contact. As a result, current conduction is linear for larger scan rates. Utilizing relation, specific capacitances for the various scan rates were determined [41],

$$C_{sp} = \frac{\int I(V)dv}{\Delta V \times v \times m}, \tag{1}$$

where "v" denotes the scan rate, "C_{sp}" is the specific capacitance of the working electrode (Fg^{-1}), and "IdV" denotes the area under the CV curve (mVs^{-1}). Similar to that, the specific capacitances are

determined by the galvanostatic charge–discharge (GCD) study utilizing the relation shown below [41],

$$C_{sp} = \frac{I * \Delta t}{m * \Delta V} \tag{2}$$

where "I" stands for discharge current density (A), "t" for discharge time (s), "m" for mass of the electrode's surface-active area (mg), and "V" for potential window range. Table 1 includes the specific capacitance determined by GCD and cyclic voltammetry. For the slower 1 Ag^{-1} scan rate, better results were seen in GCD analysis with maximum specific capacitance. Similar to cyclic voltammetry, quicker scan rates result in a decrease in some capacitances. The GCD results of NiCo$_2$O$_4$, GO/NiCo$_2$O$_4$, and N-rGO/NiCo$_2$O$_4$ are displayed in Fig. 9a–d. Scans were performed in the 1–5 Ag^{-1} range. According to

Fig. 8 Cyclic voltammetry results of **a** $NiCo_2O_4$, **b** GO/ $NiCo_2O_4$, **c** N-rGO/$NiCo_2O_4$ **d** comparison of CV curves of $NiCo_2O_4$, GO/$NiCo_2O_4$, N-rGO/$NiCo_2O_4$
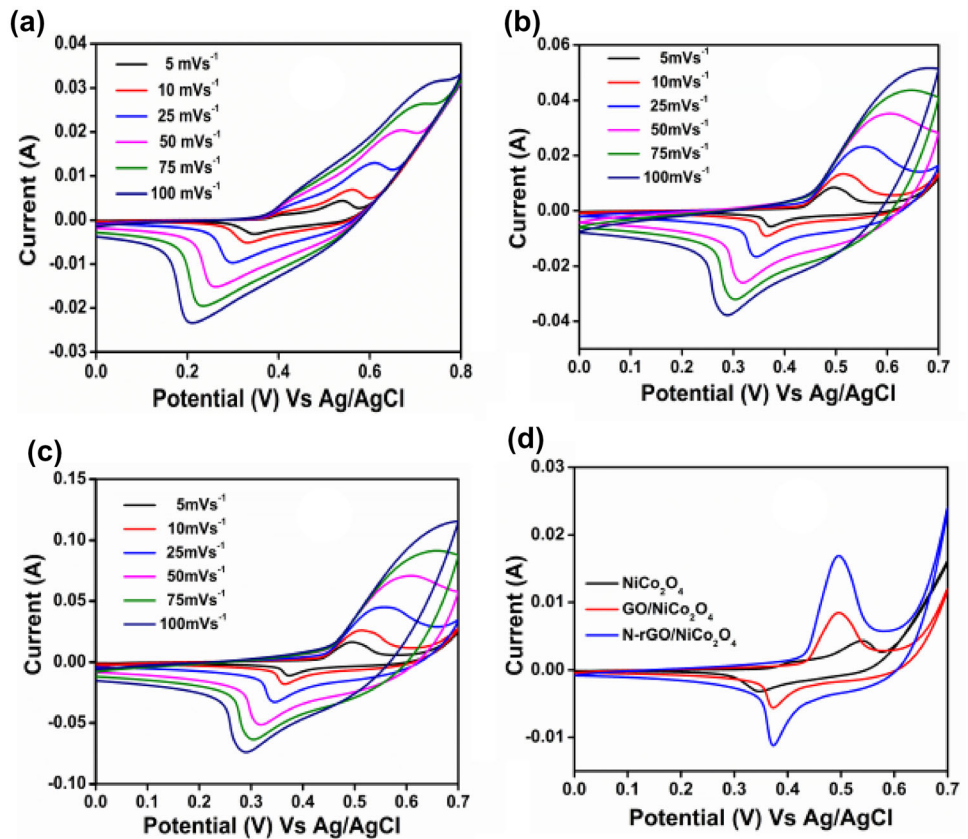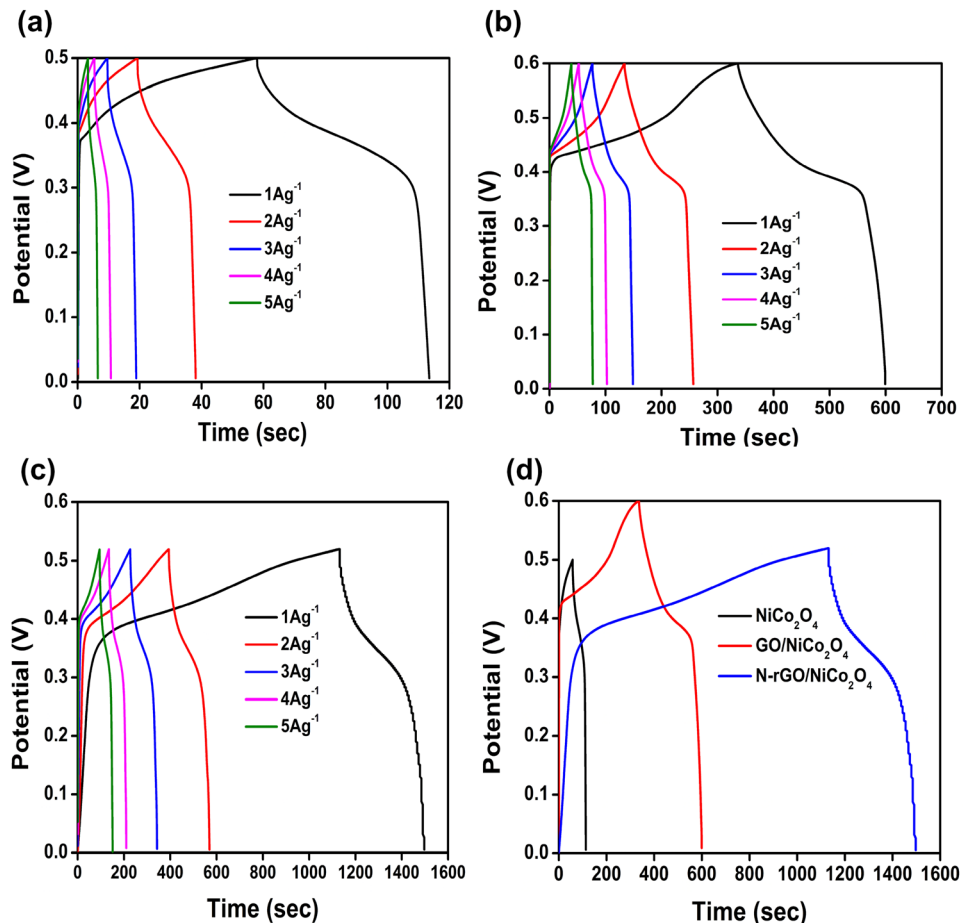

Table 1 Specific capacitances of $NiCo_2O_4$, GO/$NiCo_2O_4$, N-rGO/$NiCo_2O_4$ nanocompositesfrom CV and GCD analysis

Specific capacitances from cyclic voltammetry				Specific capacitances from GCD			
Scan rate (mVs^{-1})	$NiCo_2O_4$ (Fg^{-1})	GO/$NiCo_2O_4$ (Fg^{-1})	N-rGO/$NiCo_2O_4$ (Fg^{-1})	Current density (Ag^{-1})	$NiCo_2O_4$ (Fg^{-1})	GO/$NiCo_2O_4$ (Fg^{-1})	N-rGO/$NiCo_2O_4$ (Fg^{-1})
5	227.7	548.5	1078.2	1	111.2	533.3	701.9
10	213.2	505.3	990.3	2	75.6	412.6	689.2
25	185.8	433.	840.5	3	54	362.5	671.5
50	160.9	359.7	716.7	4	41.6	336.6	579.2
75	145.6	281.1	564.3	5	34	319.1	544.2
100	134.6	229.6	451.8	–	–	–	–

GCD curves, hybridization has resulted in a substantial increase in the discharge times of the material. The improved specific capacitance and charge-discharge duration of the N-rGO/$NiCo_2O_4$ are confirmed in Figs. 8d and 9f, which is what is required. The power and energy density of the supercapacitors are the most important parameters, notwithstanding their greater specific capacitances. The produced materials have power densities of 1250 Wkg^{-1}, 1500 Wkg^{-1}, and 1300 Wkg^{-1}, respectively, and have energy densities of 1.1 $Whkg^{-1}$, 15.9 $Whkg^{-1}$, and

20.4 $Whkg^{-1}$ for $NiCo_2O_4$, GO/$NiCo_2O_4$, and N-rGO/$NiCo_2O_4$. The redox species of Ni^{2+}/Ni^{3+} and Co^{2+}/Co^{3+} enhanced faster ionic conduction in the produced hybrid N-rGO/$NiCo_2O_4$. Due to the two-dimensional N-doped reduced graphene oxide's easy access, Fig. 9d shows a lower I_R drop than other nanomaterials generated. The comparison of specific capacitance derived from cyclic voltammetry, GCD analysis, and power, energy density for different scan rates of CV is shown in Fig. 10a–c. The curves unmistakably demonstrate that in both

Fig. 9 Galvanostatic charge-discharge results of **a** $NiCo_2O_4$, **b** GO/$NiCo_2O_4$, **c** N-rGO/$NiCo_2O_4$, **d** comparison of GCD results of $NiCo_2O_4$, GO/$NiCo_2O_4$, N-rGO/$NiCo_2O_4$


investigations, the N-rGO/$NiCo_2O_4$ has the greater specific capacitances. The nitrogen doped rGO nanocomposite has a higher power density, according to Fig. 8d of the Ragone plot for $NiCo_2O_4$, GO/$NiCo_2O_4$, and N-rGO/$NiCo_2O_4$. The study's findings unequivocally demonstrate that the nitrogen dopant in rGO can speed up ion transport. The cyclic stability of prepared nanomaterial is depicted in Fig. 10d before and after 5000 cycles. The N-rGO/$NiCo_2O_4$ nanocomposite exhibits stable performance with 90.3% retention of its original behaviour after 5000 cycles, which is higher than examined others at 10 Ag^{-1} current density. Because of the stable spinel structure of $NiCo_2O_4$, this demonstrates the reversibility of the electrode material in the cyclic process. As a result, the N-rGO/$NiCo_2O_4$ that has been developed, can be employed as an electrode material for supercapacitor applications. The energy density and power density of N-rGO/$NiCo_2O_4$ are compared to other synthesized nanomaterials in Fig. 10c of Ragone plot, with the estimated values being 26.3, 25.8, 25.2, 21.7, and 20.4 Wh kg^{-1} and 260,

520, 780, 1040, and 1300 W kg^{-1}, respectively for the N-rGO/$NiCo_2O_4$. The hybrid electrode of N-rGO/$NiCo_2O_4$ has pseudo capacitance dominant with EDLC, according to experimental results of CV and GCD.

4.2 Electrochemical impedance spectroscopy

The information about the electrode material's normal resistance and reactance is provided by the electrochemical impedance spectrum (EIS). EIS measurements were performed on each of the produced $NiCo_2O_4$, GO/$NiCo_2O_4$, and N-rGO/$NiCo_2O_4$ nanomaterial electrodes both before and after the cyclic test. Frequencies between 1 and 10^5 Hz were applied to the electrodes. Between the real and imaginary impedance parts, a plot is constructed. The solution and electrode interface's actual resistance are contained in the real component. Because there is a lot of

Fig. 10 a Comparison of CV specific capacitance of $NiCo_2O_4$, $GO/NiCo_2O_4$, N-rGO/$NiCo_2O_4$, **b** comparison of GCD specific capacitance of $NiCo_2O_4$, $GO/NiCo_2O_4$, N-rGO/$NiCo_2O_4$, **c** comparison of Ragone plot of $NiCo_2O_4$, $GO/NiCo_2O_4$, N-rGO/$NiCo_2O_4$ **d** comparison of cyclic stabilities for 5000 cycles
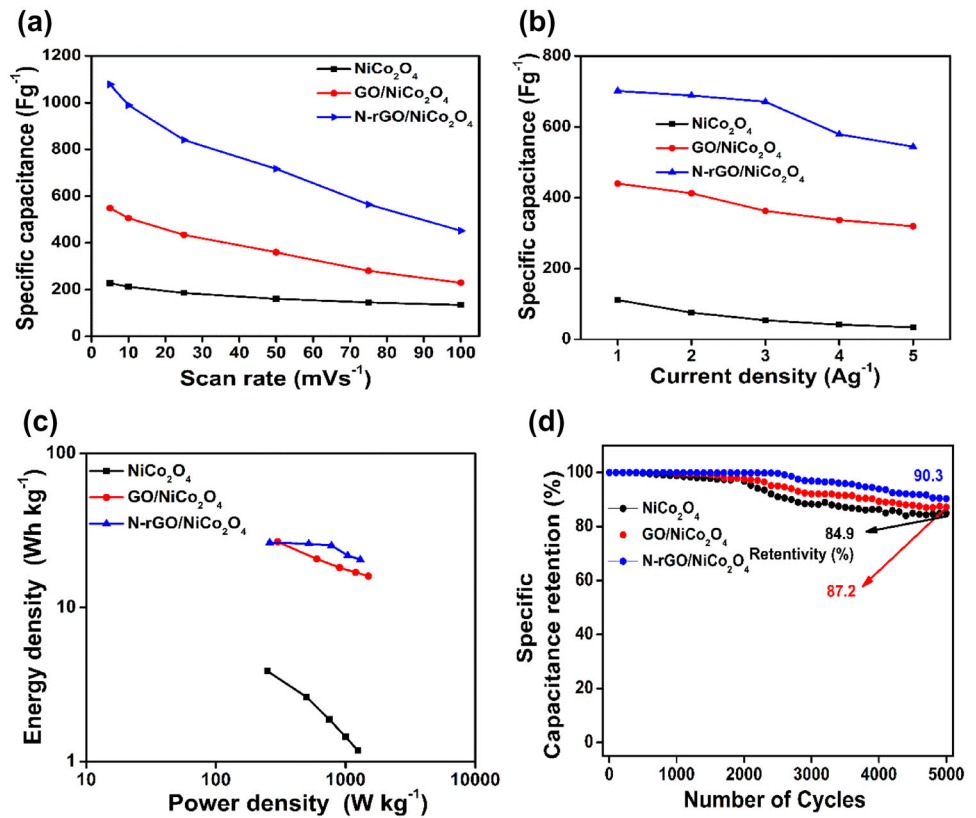
resistance at lower frequencies, the phase of the provided frequency shifts negatively, suggesting that the active material is acting inductively. The ion warming up for the frequency's application was the cause of the problem. As the applied frequency to the electrodes increases, the inductive behaviour decreases and the phase shift of the AC frequency changes to positive, indicating that the electrode material will behave capacitively at higher frequencies. The EIS spectra for the created nanomaterials are displayed in Fig. 11. It contrasts the resistance and capacitive properties of nanomaterials made of $NiCo_2O_4$, $GO/NiCo_2O_4$, and N-rGO/$NiCo_2O_4$. It should be noted that compared to other produced nanomaterials, N-rGO/$NiCo_2O_4$ exhibits extremely little resistance to the application of AC frequency and a higher capacitive attitude. Additionally, the real part's appearance did not increase linearly at the peak of the imaginary impedance. It accepted that at higher applied frequencies there was a nearly constant resistance with varying capacitive characteristics [42]. N-rGO/$NiCo_2O_4$ maintains its height for the application as a supercapacitor due to its greater specific capacitance attitude.
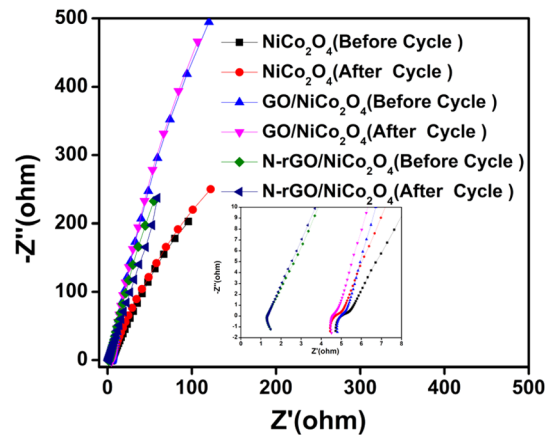
Fig. 11 Impedance analysis of $NiCo_2O_4$, $GO/NiCo_2O_4$, N-rGO/$NiCo_2O_4$ before and after cyclic test

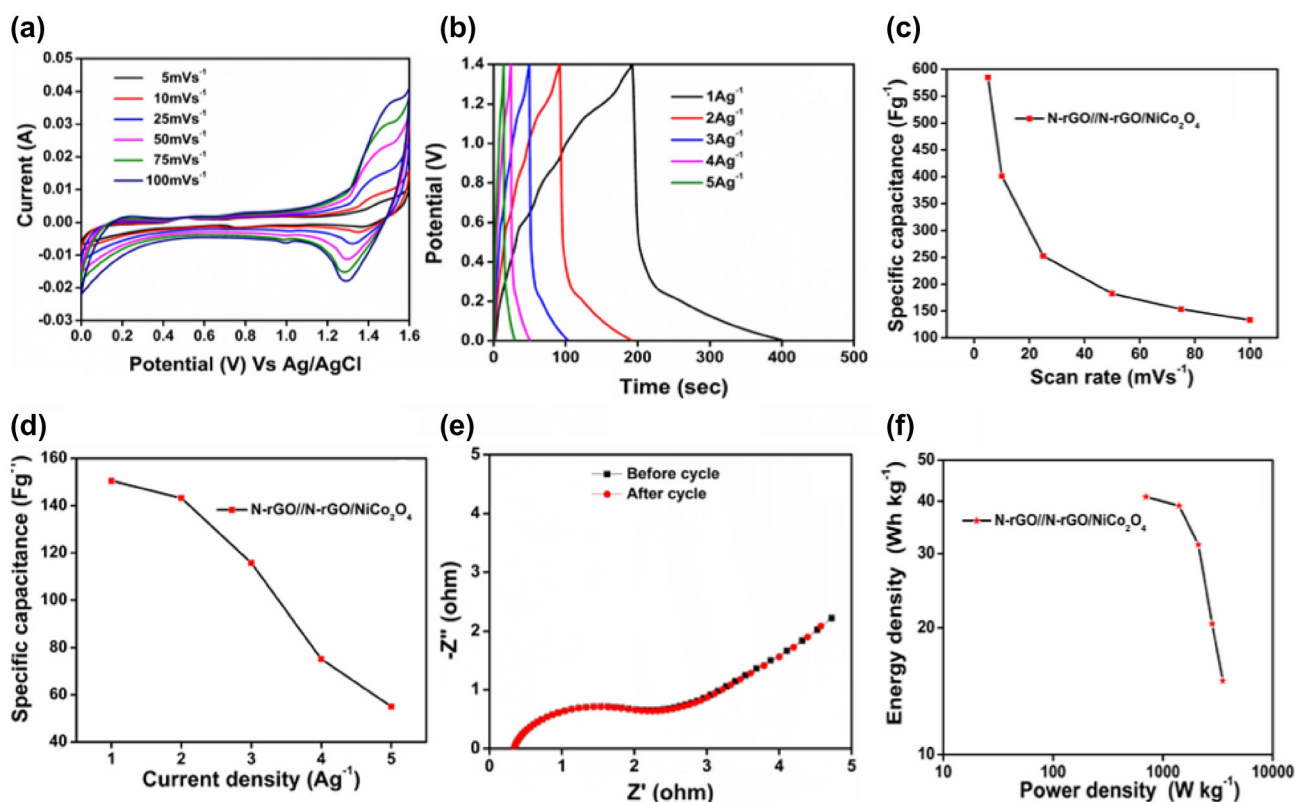## 5 Fabrication of N-rGO//N-rGO/NiCo$_2$O$_4$ asymmetric supercapacitor

A solid-state asymmetric supercapacitor with anodes of N-rGO and cathodes of N-rGO/$NiCo_2O_4$ was developed using a Whatman filter paper separator. Cyclic voltammetry, GCD, comparative specific

capacitance, and impedance of the device with energy vs. power density were compared are shown in Fig. 12a–f. The ideal range for the faradic reaction is 0 to 1.6 V. The cyclic voltammetry curves for various scan rates are shown in Fig. 12a. It demonstrates that greater scan speeds result in a larger cyclic voltammetry surface area. Equation (1) yields the following specific capacitances: 584.5, 401.2, 252.8, 182.4, 153.4, and 133.2 Fg^{-1} for scan rates of 5, 10, 25, 50, 75, and 100 mVs^{-1}. The decreased discharging time in all of the current density rates, as stated by galvanostatic charge-discharge study, is advantageous for applications involving supercapacitors. According to cyclic voltammetry and GCD curves, the decrease of certain capacitances with an increase in scan rates is consistent with the behaviour of normal electrodes. Various current densities of 1, 2, 3, and 4 Ag^{-1} at potentials ranging from 0 to 1.4 V were displayed in Fig. 12b. Even after 5000 cycles, Fig. 12e showed very low R_{CT} resistance of up to 5 ohms without any departure from the initial values. It verifies the material's capacity to conduct

electrochemistry with consistency. Maximum energy and power density of N-rGO//N-rGO/NiCo$_2$O$_4$ is shown in Ragone plot of Fig. 12f at 14.9 $Whkg^{-1}$ for 3500 Wkg^{-1}. Table 2 displays energy vs. power density for all determined cyclic voltammetry scan rates. The ASC device's cyclic stability is depicted in Fig. 13. After 5000 cycles at 10Ag^{-1}, it demonstrates roughly 90.7%, ensuring the use of the device and nanocomposite in supercapacitor applications.

6 Conclusion

By using a straightforward chemical reflux approach, hybrid GO/NiCo$_2$O$_4$, N-rGO/NiCo$_2$O$_4$ electrode nanomaterials were created. X-ray diffraction was used to confirm the crystalline phase of the NiCo$_2$O$_4$ spinel system with the Fd-3 m space group and m-3 m point group. Studies using the FTIR and Raman spectroscopies confirmed that nitrogen was incorporated into the reduced graphene oxide. By detecting the D, G bands Raman intensities and the


Fig. 12 a CV graph of N-rGO//N-rGO/NiCo$_2$O$_4$ asymmetric supercapacitor device, **b** GCD profiles of N-rGO//N-rGO/NiCo$_2$O$_4$, **c** CV specific capacitance ASC device **d** GCD

specific capacitance of ASC device, **e** Nyquist plot of ASC device **f** comparison of energy vs. power density of ASC device by Ragone plot

Table 2 Energy density vs. power density of N-rGO//N-rGO/NiCo$_2$O$_4$ asymmetric supercapacitor device

Energy density (Wh kg^{-1})	Power density (W kg^{-1})
700	40.9
1400	39
2100	31.5
2800	20.4
3500	14.9
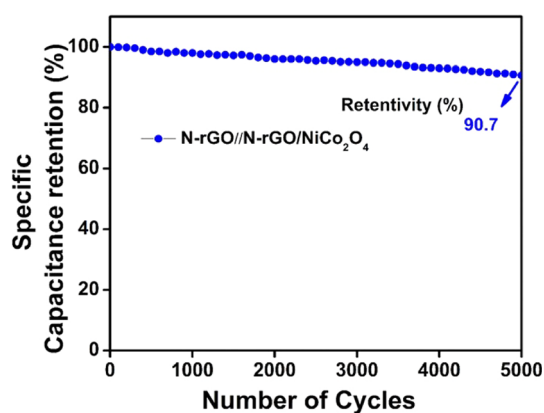
Fig. 13 Cyclic stability test of N-rGO//N-rGO/NiCo$_2$O$_4$ ASC device

shift of a wavenumber, the disorder of graphene oxide was investigated. NiCo$_2$O$_4$'s morphology, two-dimensional graphene oxide, and the surface of N-rGO were all examined. In SEM pictures, the dispersion of NiCo$_2$O$_4$ over the GO and N-rGO sheets was clearly visible. All the components are present and distributed uniformly in the nanocomposites, according to EDX and mapping analyses. The results of a cyclic voltammetry analysis in 1 M KOH showed that the specific capacitances of N-rGO/NiCo$_2$O$_4$ were 1078.2 Fg^{-1} at 5 mVs^{-1}. The hybrid active electrode material's capacitive behaviour at higher AC frequencies was confirmed by the impedance spectrum. N-rGO//N-rGO/NiCo$_2$O$_4$ asymmetric supercapacitors have been used to demonstrate higher power densities for lower energy densities with very low resistance and impedance. The cyclic stability of the N-rGO/NiCo$_2$O$_4$ nanocomposite and ASC device is greater than 90%. The N-rGO/NiCo$_2$O$_4$ material's suitability for supercapacitor applications is determined by all of its qualifications.

Acknowledgements

Author contributions

All authors contributed to the study conception and design. Materials preparation, Data curation, Investigation, Methodology, Formal analysis, Writing-Original draft was done by. GV. The experiments and results were validated by PD, NN and SS. The research work conceptualization, formal analysis, project administration, resources, supervision, writing—review & editing was done by MKK. All authors read and approved the final manuscript.

Funding

Data availability

The datasets generated during and/or analysed during the current study are available from the corresponding author on reasonable request.

Declarations

References

1. V. Ga Bui, T. Minh Tu Bui, A. Tuan Hoang, S. Nižetić, R. Sakthivel, V. Nam Tran, V. Hung Bui, D. Engel, H.

Hadiyanto, Sustain. Energy Technol. Assess. **47**, 101435 (2021)

2. C. Wang, E. Zhou, W. He, X. Deng, J. Huang, M. Ding, X. Wei, X. Liu, X. Xu, Nanomaterials **7**, 41 (2017)

3. Y. Wang, M. Zhang, Y. Li, T. Ma, H. Liu, D. Pan, X. Wang, A. Wang, Electrochim. Acta **290**, 12 (2018)

4. M.I.A. Abdel Maksoud, R.A. Fahim, A.E. Shalan, M. Abd Elkodous, S.O. Olojede, A.I. Osman, C. Farrell, A.H. Al-Muhtaseb, A.S. Awed, A.H. Ashour, D.W. Rooney, Environ. Chem. Lett. **19**, 375 (2021)

5. H. Xu, P. Song, C. Liu, Y. Zhang, Y. Du, J. Colloid Interface Sci. **530**, 58 (2018)

6. S.G. Krishnan, A. Arulraj, M. Khalid, M.V. Reddy, R. Jose, Renew. Sustain. Energy Rev. **141**, 110798 (2021)

7. M. Khan, M.N. Tahir, S.F. Adil, H.U. Khan, M.R.H. Siddiqui, A.A. Al-Warthan, W. Tremel, J. Mater. Chem. A **3**, 18753 (2015)

8. T.C. Chang, Y.T. Lu, C.H. Lee, J.K. Gupta, L.J. Hardwick, C.C. Hu, H.Y.T. Chen, ACS Omega **6**, 9692 (2021)

9. H. Jiang, J. Ma, C. Li, Chem. Commun. **48**, 4465 (2012)

10. H. Tambunan, J. Vaughan, A. D. Dalvi, W. Gordon Bacon, M. Robert, and C. Osborne, PDAC Int. Conv (2004).

11. D.P. Dubal, P. Gomez-Romero, B.R. Sankapal, R. Holze, Nano Energy **11**, 377 (2015)

12. Y. Li, X. Han, T. Yi, Y. He, and X. Li, J. Energy Chem. **31**, 54 (2019)

13. S. Manoharan, K. Krishnamoorthy, A. Sathyaseelan, S.J. Kim, Mater. Chem. Front. **5**, 6200 (2021)

14. M.R. Karim, M.M. Rahman, A.M. Asiri, S. Hayami, ACS Appl. Mater. Interfaces **12**, 10829 (2020)

15. Y. Shao, S. Zhang, M.H. Engelhard, G. Li, G. Shao, Y. Wang, J. Liu, I.A. Aksay, Y. Lin, J. Mater. Chem. **20**, 7491 (2010)

16. C. Wang, H. Hu, S. Ding, M. Dong, L. Li, Mater. Technol. **00**, 1 (2021)

17. S. Zhang, H. Gao, J. Zhou, F. Jiang, Z. Zhang, J. Alloys Compd. **792**, 474 (2019)

18. E. Mitchell, A. Jimenez, R.K. Gupta, B.K. Gupta, K. Ramasamy, M. Shahabuddin, S.R. Mishra, New. J. Chem. **39**, 2181 (2015)

19. L. Paramanik, S. Sultana, K.M. Parida, J. Colloid Interface Sci. **625**, 83 (2022)

20. S. Hassanpoor, F. Aghely, J. Iran. Chem. Soc. **18**, 993 (2021)

21. H. Liu, J. Zhu, Z. Li, Z. Shi, J. Zhu, H. Mei, Chem. Eng. J. **403**, 126325 (2021)

22. Z. Sun, Z. Yan, K. Yue, A. Li, L. Qian, Appl. Surf. Sci. **538**, 147943 (2021)

23. M.S. Islam, S.N. Faisal, L. Tong, A.K. Roy, J. Zhang, E. Haque, A.I. Minett, C.H. Wang, J. Energy Storage **37**, 102453 (2021)

24. A. Tasdemir, B. Bulut Kopuklu, A.C. Kirlioglu, S. Alkan, Gursel, A. Yurum, Int. J. Hydrogen Energy **46**, 11865 (2021)

25. W.S. Hummers, R.E. Offeman, J. Am. Chem. Soc. **80**, 1339 (1958)

26. O. Knop, K.I. Reid, Sutarno, Y. Nakagawa, Can. J. Chem. **46**, 3463 (1968). https://doi.org/10.1139/V68-576

27. G. Vignesh, R. Ranjithkumar, P. Devendran, N. Nallamuthu, S. Sudhahar, M. Krishna Kumar, Mater. Sci. Eng. B **290**, 116328 (2023)

28. C.J. Bartel, A. Trewartha, Q. Wang, A. Dunn, A. Jain, G. Ceder, NPJ Comput. Mater. **61**, 6 (2020)

29. X. Sun, J. Sun, L. Guo, L. Hou, C. Yuan, RSC Adv. **10**, 35611 (2020)

30. A. Misra, P.K. Tyagi, M.K. Singh, D.S. Misra, Diam. Relat. Mater. **15**, 385 (2006)

31. M. Rybin, A. Pereyaslavtsev, T. Vasilieva, V. Myasnikov, I. Sokolov, A. Pavlova, E. Obraztsova, A. Khomich, V. Ralchenko, E. Obraztsova, Carbon N. Y **96**, 196 (2016)

32. D. Geng, S. Yang, Y. Zhang, J. Yang, J. Liu, R. Li, T.K. Sham, X. Sun, S. Ye, S. Knights, Appl. Surf. Sci. **257**, 9193 (2011)

33. D. He, Z. Peng, W. Gong, Y. Luo, P. Zhao, L. Kong, RSC Adv. **5**, 11966 (2015)

34. V. Țucureanu, A. Matei, A.M. Avram, and V. Vasilica, Vasilica țucureanu. Crit. Rev. Anal. Chem. **46**, 502 (2016)

35. A.Y. Lee, K. Yang, N.D. Anh, C. Park, S.M. Lee, T.G. Lee, M.S. Jeong, Appl. Surf. Sci. **536**, 147990 (2021)

36. K.N. Kudin, B. Ozbas, H.C. Schniepp, R.K. Prud'homme, I.A. Aksay, R. Car, Nano Lett. **8**, 36 (2008)

37. S. Claramunt, A. Varea, D. López-Díaz, M.M. Velázquez, A. Cornet, A. Cirera, J. Phys. Chem. C **119**, 10123 (2015)

38. R. Larciprete, S. Fabris, T. Sun, P. Lacovig, A. Baraldi, S. Lizzit, J. Am. Chem. Soc. **133**, 17315 (2011)

39. X. Qiao, S. Liao, G. Wang, R. Zheng, H. Song, X. Li, Carbon **99**, 272 (2016)

40. K.C. Tsay, L. Zhang, J. Zhang, Electrochim. Acta **60**, 428 (2012)

41. S. EzhilArasi, R. Ranjithkumar, P. Devendran, M. Krishnakumar, A. Arivarasan, J. Mater. Sci. Mater. Electron. **31**, 7012 (2020)

42. P.L. Taberna, C. Portet, P. Simon, Appl. Phys. A **824**(82), 639 (2005)